Nano Research
DOI 10.1007/s12274-017-1433-6
Research Article

ISSN 1998-0124
CN 11-5974/O4

Interface-modulated fabrication of hierarchical yolk–shell Co_3O_4/C dodecahedrons as stable anodes for lithium and sodium storage

Yuzhu Wu[1,§], Jiashen Meng[1,§], Qi Li[1] (✉), Chaojiang Niu[1], Xuanpeng Wang[1], Wei Yang[1], Wei Li[1], and Liqiang Mai[1,2] (✉)

[1] *State Key Laboratory of Advanced Technology for Materials Synthesis and Processing, Wuhan University of Technology, Wuhan 430070, China*
[2] *Department of Chemistry, University of California, Berkeley, California 94720, USA*
[§] *These authors contributed equally to this work.*

Received: 30 September 2016
Revised: 5 December 2016
Accepted: 21 December 2016

KEYWORDS

carbon-based metal oxide, metal–organic frameworks (MOFs), yolk–shell structure, lithium-ion batteries (LIBs), sodium-ion batteries (SIBs)

ABSTRACT

Transition-metal oxides (TMOs) have gradually attracted attention from researchers as anode materials for lithium-ion batteries (LIBs) and sodium-ion batteries (SIBs) because of their high theoretical capacity. However, their poor cycling stability and inferior rate capability resulting from the large volume variation during the lithiation/sodiation process and their low intrinsic electronic conductivity limit their applications. To solve the problems of TMOs, carbon-based metal-oxide composites with complex structures derived from metal–organic frameworks (MOFs) have emerged as promising electrode materials for LIBs and SIBs. In this study, we adopted a facile interface-modulated method to synthesize yolk–shell carbon-based Co_3O_4 dodecahedrons derived from ZIF-67 zeolitic imidazolate frameworks. This strategy is based on the interface separation between the ZIF-67 core and the carbon-based shell during the pyrolysis process. The unique yolk–shell structure effectively accommodates the volume expansion during lithiation or sodiation, and the carbon matrix improves the electrical conductivity of the electrode. As an anode for LIBs, the yolk–shell Co_3O_4/C dodecahedrons exhibit a high specific capacity and excellent cycling stability (1,100 $mAh\cdot g^{-1}$ after 120 cycles at 200 $mA\cdot g^{-1}$). As an anode for SIBs, the composites exhibit an outstanding rate capability (307 $mAh\cdot g^{-1}$ at 1,000 $mA\cdot g^{-1}$ and 269 $mAh\cdot g^{-1}$ at 2,000 $mA\cdot g^{-1}$). Detailed electrochemical kinetic analysis indicates that the energy storage for Li^+ and Na^+ in yolk–shell Co_3O_4/C dodecahedrons shows a dominant capacitive behavior. This work introduces an effective approach for fabricating carbon-based metal-oxide composites by using MOFs as ideal precursors and as electrode materials to enhance the electrochemical performance of LIBs and SIBs.

Address correspondence to Liqiang Mai, mlq518@whut.edu.cn; Qi Li, qi.li@whut.edu.cn

TSINGHUA UNIVERSITY PRESS Springer

1 Introduction

With the rapid development of portable electronic devices, electric vehicles (EVs), hybrid EVs, and large-scale smart grids, energy-storage systems with a high capacity, high efficiency, long service life, high safety, and low cost are urgently needed [1–3]. Among the various energy-storage technologies, rechargeable batteries are the most promising, with a high energy-conversion efficiency and long lifespan for energy-storage systems [4–8], including lithium-ion batteries (LIBs) and sodium-ion batteries (SIBs). The energy densities of LIBs mainly depend on the capacities and operating potentials of the electrode materials [9–11]. Graphite, which is the most common anode material in commercial LIBs, has a limited theoretical specific capacity of 372 $mAh \cdot g^{-1}$ [10] and hardly meets the requirements of future energy-storage systems. Transition-metal oxides have attracted considerable attention as emerging anode materials owing to their high theoretical capacities (>600 $mAh \cdot g^{-1}$) [11–16] associated with reversible redox reactions compared with commercial graphite. However, the intrinsic drawbacks of transition-metal oxides, including their poor electrical conductivity and large volume variation during lithiation/delithiation [17], lead to slow reaction kinetics and the pulverization of electrodes, causing a poor rate capability and a large irreversible capacity loss. SIBs are potential alternatives to LIBs for large-scale energy storage because of their low cost and the abundance of sodium [18–21]. However, the Na^+ ion (1.06 Å) is larger than Li^+ (0.76 Å), resulting in more severe volume expansion and far slower kinetics in conversion reactions. Therefore, it is a great challenge to obtain transition-metal oxide-based anode materials that can accommodate the volume expansion and conductivity enhancement for both LIBs and SIBs.

Intensive efforts have been directed towards the development of efficient strategies for the design and synthesis of micro/nanostructural transition-metal oxides. One typical method involves fabricating unique structures such as porous/hollow materials (especially those with complex interiors), which can not only shorten the Li^+/Na^+ diffusion pathways and increase the electrode–electrolyte contact areas but also provide additional interior space to accommodate volume variation [22–25]. Another solution is to combine transition-metal oxides with carbonaceous materials (e.g., porous carbon, carbon nanotubes, graphene [26–31], or conducting polymers [32]) to enhance the conductivity and buffer the strain from volume changes. Wang et al. [33] reported a three-dimensional nanoporous Co_3O_4/C hybrid electrode with excellent capacitive performances for supercapacitors. Despite the great successes of both the aforementioned strategies, it remains very challenging to develop a facile and general method for synthesizing carbon-based hollow or more complex structures and thereby realize the merits of the two strategies for LIBs and SIBs.

Metal–organic frameworks (MOFs) have been widely used as sacrificial templates to synthesize various porous carbons and metal oxides [10, 23, 34–36]. Moreover, MOF-derived materials can be readily used as electrodes for high-performance electrochemical energy storage. For instance, Shao et al. [35] and Han et al. [37] reported a two-step calcination method for preparing Co_3O_4 hollow dodecahedrons derived from Co-MOFs. Tian et al. [38] reported the synthesis of porous Co_3O_4 hollow tetrahedrons through the thermolysis of Co-based MOFs. Despite their improved lithium-storage capabilities, their rate capabilities were unsatisfactory. Hou et al. [39] adopted a facile method to synthesize a novel Co_3O_4/N-doped porous carbon hybrid with a dodecahedral structure through the two-step thermal transformation of a cobalt-based zeolitic imidazolate framework. This hybrid exhibited superior electrochemical performances, including an excellent rate capability and outstanding cycling stability. Zhu et al. [40] presented hierarchical hollow NiO/Ni/graphene composites that were prepared from intrinsic hollow Ni-MOFs and exhibited superior performances in LIBs and SIBs. Therefore, the development of a facile method for synthesizing complex carbon-based metal-oxide structures derived from MOFs for high-performance rechargeable batteries is highly desired.

In this study, by using cobalt-based ZIF-67 as a single precursor, we developed a facile interface-modulated approach for the fabrication of hierarchical yolk–shell Co_3O_4/C dodecahedrons by controlling a two-step heat-treatment process. This strategy employs the interface separation between the ZIF-67 core and the carbon-based shell during pyrolysis to obtain the yolk–shell structure. Co_3O_4 nanoparticles are embedded *in situ* in the carbon matrix. The whole matrix is regarded as the shell, and the analogous spherical Co_3O_4 nanoparticles reunite as the core. The synthesized yolk–shell Co_3O_4/C dodecahedrons exhibit a high specific capacity, excellent cycling stability, and outstanding rate capability in LIBs and SIBs. Our preliminary investigation indicates that the composites are promising materials for lithium- and sodium-storage devices.

2 Experimental

2.1 Material synthesis

2.1.1 Preparation of ZIF-67 rhombic dodecahedral microcrystals

All the chemical reagents used were of analytical grade, without further purification. We dissolved 1 mmol of cobalt nitrate hexahydrate and 4 mmol of 2-methylimidazole separately in 25 mL of methanol. The latter clear solution was poured into the former pink solution under stirring at room temperature. After 24 h, purple powders were collected by centrifugation, washed with methanol three times, and dried at 70 °C in air for 6 h.

2.1.2 Preparation of yolk–shell Co_3O_4/C dodecahedrons and bulk Co_3O_4

The ZIF-67 precursor was placed in a tube furnace and heated to 450 °C at 5 $°C\cdot min^{-1}$ in an argon atmosphere for 2 h. Then, the primary product was annealed at 270 °C (5 $°C\cdot min^{-1}$) in air. Yolk–shell Co_3O_4/C dodecahedrons were obtained. As a control experiment, bulk Co_3O_4 was synthesized by sintering ZIF-67 directly at 350 °C (5 $°C\cdot min^{-1}$) in air for 3 h.

2.1.3 Preparation of yolk–shell NiO/C microspheres

In a typical preparation procedure described by Zhu et al. [40], 0.43 g of nickel nitrate hexahydrate and 0.15 g of 1,3,5-benzenetricarboxylic (BTC) were dissolved in a mixture solution containing 10 mL of distilled water, 10 mL of ethanol, and 10 mL of dimethylformamide under vigorous stirring. Then, 1.5 g of polyvinylpyrrolidone was added, and the mixture was stirred at room temperature for 1 h. The obtained light-green solution was transferred to a 50-mL Teflon-lined autoclave and aged at 150 °C for 1 h. Ni-BTC microspheres were collected after washing with alcohol three times and drying at 70 °C in air for 6 h. The precursor was sintered at 400 °C (5 $°C\cdot min^{-1}$) in argon for 1 h. Then, the primary product was annealed at 270 °C (5 $°C\cdot min^{-1}$) in air for 3 h. Yolk–shell NiO/C microspheres were obtained.

2.2 Characterization

X-ray diffraction (XRD) measurements were performed to obtain crystallographic information using a D8 Discover X-ray diffractometer with a Cu Kα X-ray source. Field-emission scanning electron microscopy (FESEM) images were collected using a JEOL-7100F microscope. Raman spectra were acquired using a Renishaw RM-1000 laser Raman microscope. Thermogravimetric (TG) analysis was performed using an STA 449 C. Energy-dispersive X-ray spectra were recorded using an Oxford IE250 system. X-ray photoelectron spectroscopy (XPS) was performed using a VG MultiLab 2000 instrument. Transmission electron microscopy (TEM) and high-resolution TEM (HRTEM) images were recorded using a JEOL JEM-2100F transmission electron microscope. The Brunauer–Emmett–Teller surface areas were calculated according to nitrogen-adsorption isotherms measured at 77 K using a Trwastar-3020 instrument.

2.3 Electrochemical characterization

The electrochemical properties were characterized by assembling 2016 coin cells in a glove box filled with pure argon. The anode electrodes were composed of 70 wt.% active materials, 20 wt.% acetylene black, and 10 wt.% carboxymethyl cellulose binder. After being coated onto a copper foil, the electrode film was uniformly cut into round slices (~0.8 cm^2, area) weighing a total of ~1.2 mg. The corresponding areal mass loading was 1.5 $mg\cdot cm^{-2}$. For LIBs, lithium foil was used as the counter electrode, and the separator was a Celgard 2400 microporous membrane. The electrolyte was a 1 M lithium hexafluorophosphate

($LiPF_6$) solution in ethylene carbon (EC)-dimethyl carbonate (DMC) (1:1 w/w). For SIBs, sodium metal was used as the counter electrode, a 1 M solution of $NaClO_4$ in EC and DMC (1:1 v/v) with 5% fluoroethylene carbonate (FEC) additive and without the FEC additive were used as the electrolyte, and a Whatman glass fiber (GF/D) was used as the separator. Galvanostatic charge/discharge measurements were performed using a multichannel battery-testing system (LAND CT2001A). Cyclic voltammetry (CV) and electrochemical impedance spectroscopy (EIS) were performed using a CHI 600e electrochemical workstation and Autolab PGSTAT 302N, respectively.

3 Results and discussion

ZIF-67 was selected as the precursor for synthesizing carbon-based Co_3O_4. The overall synthesis procedure was designed by controlling the two-step heat-treatment process (Fig. 1). First, the phase of the as-prepared ZIF-67 was confirmed by the XRD pattern (Fig. 2(a)). All the diffraction peaks well matched those simulated for ZIF-67, as well as the pattern reported in Ref. [41]. The material exhibited the morphology of a rhombic dodecahedron with a smooth surface (Figs. 2(b) and 2(c)) and had a surface area of 1,389.6 $m^2 \cdot g^{-1}$ (Fig. S1(a) in the Electronic Supplementary Material (ESM)), suggesting its highly developed porous structure. TG curves of ZIF-67 dodecahedrons are shown in Fig. S1(b) in the ESM. The ZIF-67 exhibited obvious weight loss when heated to 360 °C in air and 500 °C in a nitrogen atmosphere.

On the basis of the TG analysis results, a facile interface-modulated calcination method for fabricating hierarchical yolk–shell Co_3O_4/C was developed (Fig. 1). ZIF-67 dodecahedrons were first sintered at 450 °C in argon to obtain yolk–shell ZIF-67/C dodecahedrons. At this stage, because the pyrolysis direction was from the outside to the inside [42], the organic ligands on the ZIF-67 surface were preferentially carbonized, and a carbon-based shell formed. The large volume change from ZIF-67 to the carbon-based composite led to considerable shrinkage of the inner core, modulating the interface separation. Because the temperature was not high enough for ZIF-67 to decompose completely, the inner core was still ZIF-67 (demonstrated by the XRD pattern shown in Fig. 2(d)). In the heterogeneous contraction process caused by non-equilibrium heat treatment [35], voids between the carbon-based shell and ZIF-67 core were generated (Fig. 2(e)), and an initial yolk–shell intermediate (denoted as ZIF-67/C) was formed. The polyhedral morphology of the yolk–shell ZIF-67/C was perfectly maintained after the first step of the calcination process (Fig. 2(f)). The yolk–shell structure of cracked ZIF-67/C is clearly observed in the SEM image (Fig. 2(e)).

The ZIF-67/C was then annealed at 270 °C for 3 h in air. As the inner ZIF-67 decomposed rapidly, the inner core, which was assembled with Co_3O_4 nanoparticles (10–30 nm) as shown in Fig. S3 in the ESM, was formed. At this relatively low temperature, the carbon in the outer shell was not completely oxidized, and Co_3O_4 nanoparticles (10–30 nm) were *in situ* anchored in the shell (Figs. 3(d)–3(f)). Finally, hierarchical yolk–shell carbon-based Co_3O_4 (denoted as yolk–shell Co_3O_4/C) dodecahedrons were obtained.

The XRD pattern of the yolk–shell Co_3O_4/C dodecahedrons confirms that a pure Co_3O_4 spinel phase with a face-centered cubic lattice (JCPDS No. 42-1467, space group: *Fd*3*m*, cell parameter a = 8.084 Å) was obtained (Fig. 3(a)). The diffraction peaks of the yolk–shell composite are lower in intensity and broader

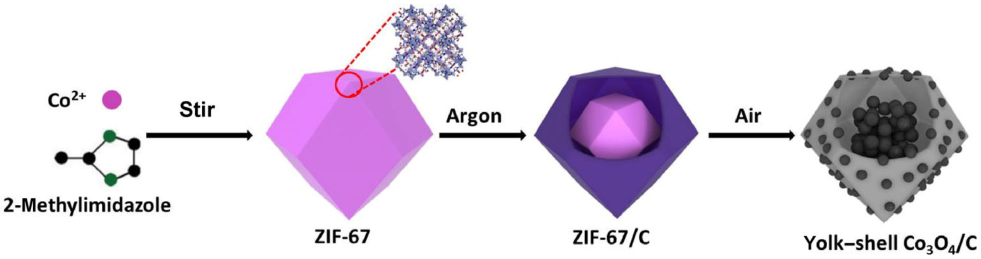

Figure 1 Schematic of ZIF-67-derived hierarchical yolk–shell Co_3O_4/C dodecahedrons. ZIF-67 was heated at 450 °C for 2 h in an argon atmosphere to obtain ZIF-67/C, and then the sample was annealed at 270 °C for 3 h in air to obtain yolk–shell Co_3O_4/C.

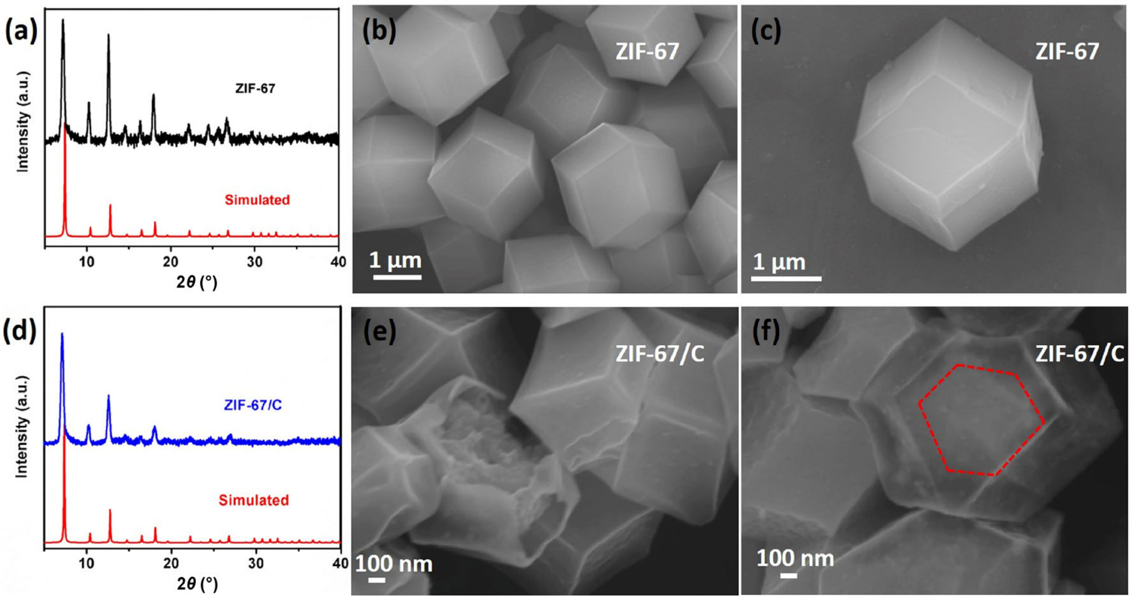

Figure 2 (a) XRD patterns of the as-synthesized ZIF-67 dodecahedrons and simulated ZIF-67. ((b) and (c)) SEM images of the as-synthesized ZIF-67 dodecahedrons. (d) XRD patterns of yolk–shell ZIF-67/C dodecahedrons and simulated ZIF-67. ((e) and (f)) SEM images of yolk–shell ZIF-67/C dodecahedrons.

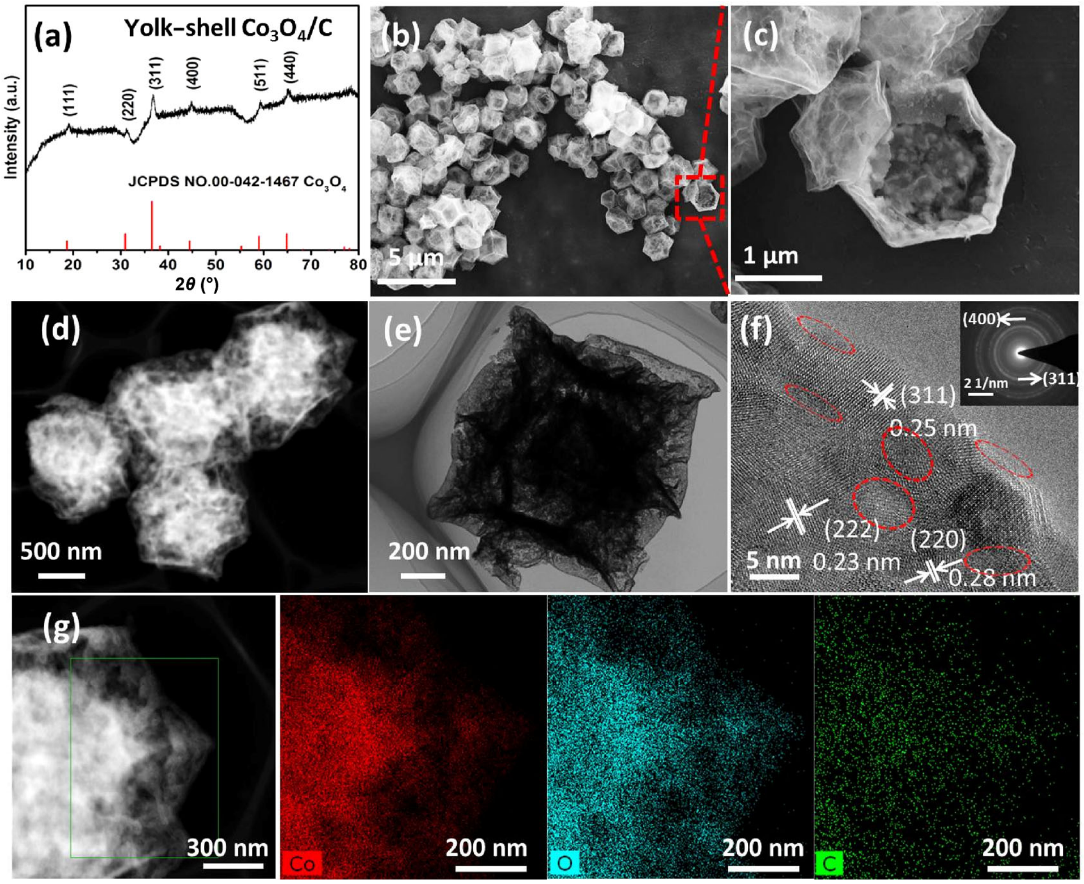

Figure 3 (a) XRD pattern of yolk–shell Co_3O_4/C dodecahedrons obtained from the thermolysis of ZIF-67/C. SEM ((b) and (c)), STEM–HAADF (d), TEM (e), and HRTEM (f) images of yolk–shell Co_3O_4/C. The inset of (f) shows the SAED pattern. (g) STEM image of yolk–shell Co_3O_4/C and the corresponding STEM–EDS mappings for Co, O, and C.

than those of bulk Co_3O_4 (denoted as Co_3O_4-B) (Fig. S2(a) in the ESM), which indicates the lower crystallinity and smaller grain size of the Co_3O_4. No obvious diffraction peak of carbon is detected, which is ascribed to the amorphous nature of the carbon shell. The material retained the size and overall structure of ZIF-67 after calcination (Fig. 3(b)). The magnified SEM image shown in Fig. 3(c) reveals the yolk–shell structure of the final products, whose interior contained many aggregated analogous spherical particles as well as a large void between the shell and the core. The scanning-TEM high-angle annular dark-field (STEM–HAADF) image shown in Fig. 3(d) and the TEM image shown in Fig. 3(e) confirm the yolk–shell structure. The HRTEM image of the area near the dodecahedron edge indicates distinct lattice fringes with interlayer spacings of 0.23, 0.25, and 0.28 nm, which are in accordance with the (222), (311), and (220) lattice planes of Co_3O_4, respectively. The positions of the carbon in the shell are highlighted by the red dotted line in Fig. 3(f). The selected-area electron diffraction (SAED) pattern shown in the inset of Fig. 3(f) indicates the polycrystalline features of the Co_3O_4 dodecahedrons. The STEM–energy-dispersive spectroscopy (STEM–EDS) mappings shown in Fig. 3(g) confirm the uniform distribution of Co, O, and C. However, the SEM image shown in Fig. S2(b) of the ESM indicates that Co_3O_4-B consisted of large particles with a crinkled surface. The XPS results indicate the valence states of the elements in the yolk–shell composites (Fig. S4 in the ESM). The two peaks of the Co 2p spectrum centered at 780.7 and 795.9 eV correspond to Co $2p_{3/2}$ and Co $2p_{1/2}$ (Fig. S4(b) in the ESM). The gap between the peaks is ~15 eV (spin-orbit splitting), which corresponds to the standard Co_3O_4 spectra [43].

The yolk–shell Co_3O_4/C dodecahedrons exhibited a large surface area of 179.4 $m^2 \cdot g^{-1}$ and a total pore volume of 0.3 $cm^3 \cdot g^{-1}$, as characterized by the nitrogen adsorption–desorption isotherm (Fig. S5(a) in the ESM). The corresponding pore-size distribution curve clearly reveals that the material had abundant mesopores with diameters mostly concentrated at 3.8, 5.3, and 25.8 nm (Fig. S5(b) in the ESM). The mesopores are attributed to the liberation of gases during the oxidation decomposition of organic ligands in the pyrolysis. The Raman spectrum (Fig. S6 in the ESM) indicates that the carbon in Co_3O_4/C dodecahedrons was partially graphitized. The mass content of carbon in the yolk–shell Co_3O_4/C dodecahedrons was ~6.45 wt.% (Fig. S7 in the ESM).

To confirm the general applicability of our strategy, yolk–shell NiO/C microspheres were also fabricated by annealing Ni-BTC (Fig. S8 in the ESM). The broken microspheres exhibit the yolk–shell structure. This interface-modulated two-step sintering strategy can be applied for synthesizing yolk–shell structures for other metal oxides.

The electrochemical performances of the yolk–shell Co_3O_4/C dodecahedrons in LIBs were tested. The CV curves of the electrode were measured in the range of 0.01 to 3 V vs. Li^+/Li at a scan rate of 0.1 $mV \cdot s^{-1}$ (Fig. 4(a)). In the first cycle, there was an intense peak around 0.8 V in the discharge process, corresponding to the initial reduction of Co_3O_4 to metallic cobalt, accompanied by the formation of Li_2O [44]. A broad peak at ~2.1 V appeared in the charge process, which is ascribed to the formation of cobalt oxide [39]. In the second cycle, two prominent peaks were observed at 0.85 and 1.3 V, which are attributed to the multistep reduction reactions of Co_3O_4 with Li^+, while the position of the oxidation peak remained almost unchanged [45]. The subsequent CV curves exhibit good reproducibility and overlap, indicating the good reversibility of the electrochemical reactions. According to the galvanostatic charge/discharge profiles of the yolk–shell Co_3O_4/C dodecahedrons measured at a current density of 200 $mA \cdot g^{-1}$ (Fig. 4(b)), the first discharge and charge capacities were 1,209 and 864 $mAh \cdot g^{-1}$, respectively, corresponding to a Coulombic efficiency of ~71%. An irreversible capacity loss occurred in the first cycle, which is ascribed to the formation of solid-electrolyte interphase (SEI) films, a Li_2O phase, and the irreversible decomposition of the electrolyte [44]. As shown in Fig. 4(c), the discharge capacity of the yolk–shell Co_3O_4/C dodecahedrons increased gradually until ~40 cycles, remained stable for the subsequent cycles, and finally reached 1,100 $mAh \cdot g^{-1}$ after 120 cycles. This phenomenon has been observed for several other transition-metal oxides and is attributed to the activation and growth of an electrochemical gel-like polymer layer [46–50], which can enhance the lithium-

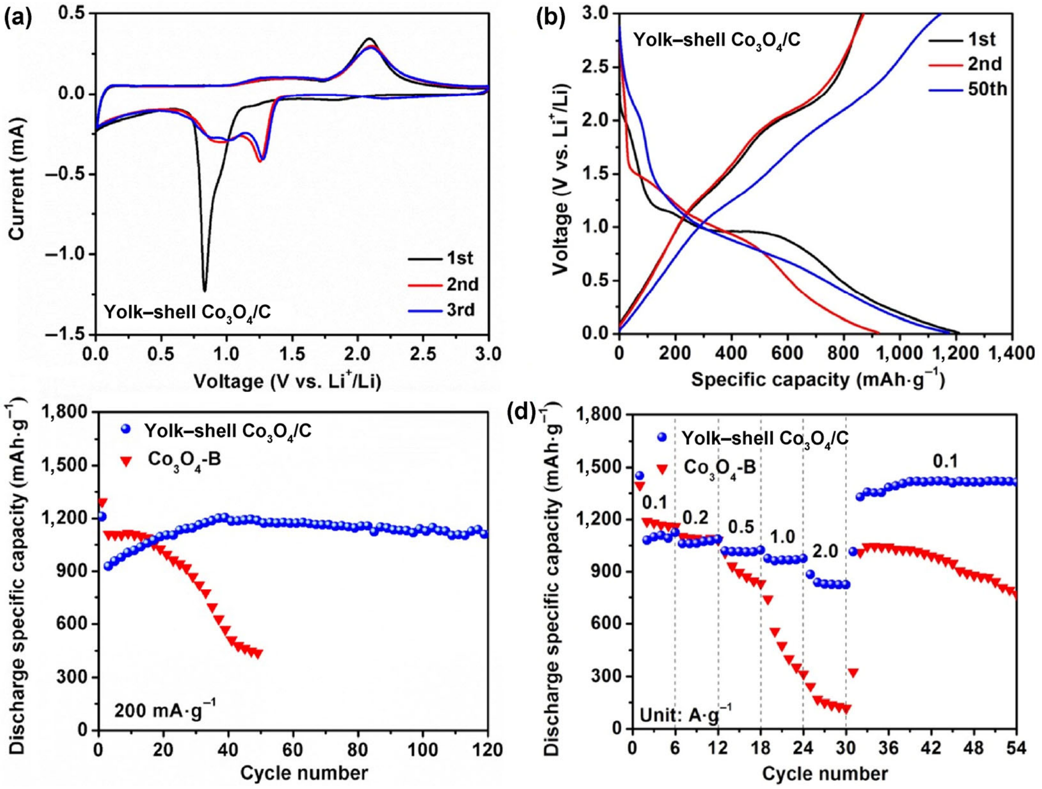

Figure 4 Electrochemical performances of yolk–shell Co_3O_4/C dodecahedrons in LIBs. (a) CV curves of yolk–shell Co_3O_4/C dodecahedrons collected at a scan rate of 0.1 mV·s^{-1} within the voltage range of 0.01–3 V. (b) Galvanostatic charge/discharge profiles at a current density of 200 mA·g^{-1}. (c) Cycling performance of the yolk–shell Co_3O_4/C dodecahedrons and Co_3O_4-B at a current rate of 200 mA·g^{-1}. (d) Comparison of the capacities with respect to the cycle number for yolk–shell Co_3O_4/C dodecahedrons and Co_3O_4-B at various current densities ranging from 0.1 to 2.0 A·g^{-1}.

ion storage. The SEM image after cycling at 200 mA·g^{-1} for 50 cycles shows no notable variation in morphology (Fig. S9 in the ESM), confirming the cycling stability for LIBs. Compared with the yolk–shell Co_3O_4/C dodecahedrons, the Co_3O_4-B exhibited a lower capacity of only 400 mAh·g^{-1} after 50 cycles. In addition to the high capacity and stable cycling performance, the yolk–shell Co_3O_4/C dodecahedrons exhibited a better rate capability than Co_3O_4-B (Fig. 4(d)). The average discharge specific capacities were 1,125, 1,086, 1,023, 975, and 826 mAh·g^{-1} at 100, 200, 500, 1,000, and 2,000 mA·g^{-1}, respectively. When the current density returned to 100 mA·g^{-1}, a discharge capacity of 1,415 mAh·g^{-1} was recovered, suggesting that no capacity decays occurred but that there were increases after cycling at a high current density. The EIS results for the yolk–shell Co_3O_4/C dodecahedrons and Co_3O_4-B are shown in Fig. S10 in the ESM. The semicircle of the yolk–shell Co_3O_4/C dodecahedrons is smaller than that of Co_3O_4-B, indicating the lower charge-transfer resistance of the yolk–shell Co_3O_4/C dodecahedrons. The steeper line of the EIS curve in the low-frequency region indicates that the lithium-ion diffusion of the yolk–shell Co_3O_4/C dodecahedrons was faster than that of Co_3O_4-B. This result confirms that the yolk–shell Co_3O_4/C had better electrical conductivity, which resulted in a better electrochemical performance compared with Co_3O_4-B. Overall, the results demonstrate that the yolk–shell Co_3O_4/C dodecahedrons are promising anodes with a high specific capacity and rate capability for LIBs (Table S1 in the ESM [39, 44, 45, 51]).

To clarify the mechanism underlying the excellent rate capability and cycling stability, the electrochemical kinetics were investigated [52, 53]. The CV curves measured after the first cycle all exhibit similar shapes, and the gradual broadening of the peaks is observed, which is similar to the feature of pseudocapacitive materials (Fig. 5(a)). Thus, a related analysis was performed regarding the behavior of the peak current by assuming that the current (i) obeyed a power-law relationship with the sweep rate (ν), as shown in the following equation

$$i = a\nu^{b} \tag{1}$$

where a is a constant. A b value of 0.5 indicates a completely diffusion-controlled process, whereas b = 1.0 represents a capacitive process [54]. By plotting log i vs. log ν, the b values are calculated to be 0.86 and 0.88 for the cathodic and anodic peaks, respectively (Fig. 5(b)), indicating that the majority of the current at the peak potential is capacitive. This result demonstrates that the capacitive behavior dominates the reaction of the yolk–shell Co_3O_4/C dodecahedrons with relatively fast kinetics.

To be more precise, the relationship in Eq. (1) can be divided into two parts corresponding to the capacitive ($k_1\nu$) and diffusion-limited effects ($k_2\nu^{1/2}$), as follows [55]

$$i = k_1\nu + k_2\nu^{1/2} \tag{2}$$

where k_1 and k_2 are constants for a given potential. By plotting $i/\nu^{1/2}$ vs. $\nu^{1/2}$, k_1 is determined as the slope, and k_2 is determined as the intercept; therefore, the capacitive and diffusion contributions can be obtained. At a scan rate of 0.8 mV·s^{-1} (Fig. 5(c)), ~54% of the total current, i.e., the capacity, is capacitive in nature. Similarly, the contribution ratios between the two different processes at other scan rates were calculated (Fig. 5(d)). The quantified results show that the capacitive contribution gradually improves with an increasing scan rate. The pseudocapacitive contribution (red region) is characterized by broad peaks, which are characteristic of surface-confined charge storage [56]. As observed in Co_3O_4/C, the diffusion-controlled currents are located predominantly in the peak regions of the CV curves, as redox peaks are expected

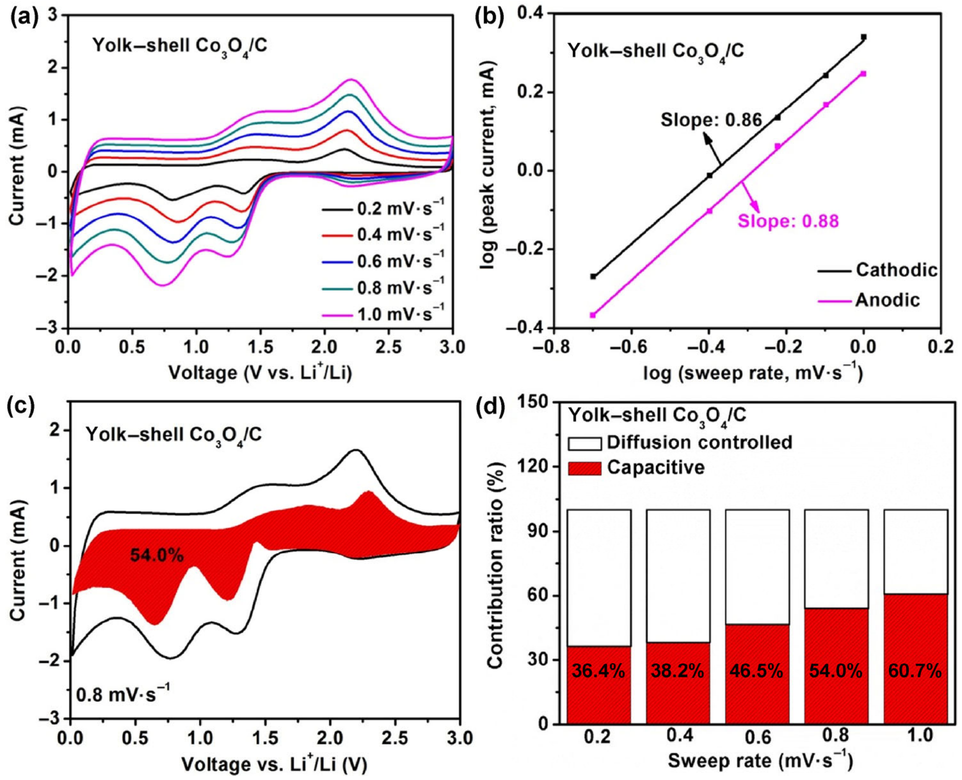

Figure 5 Kinetic analysis of the electrochemical behavior vs. Li$^+$/Li for the yolk–shell Co_3O_4/C dodecahedrons. (a) CV curves at various scan rates ranging from 0.2 to 1 mV·s^{-1}. (b) Determination of the b value using the relationship between the peak current and the scan rate according to the voltammograms in (a). (c) Separation of the capacitive and diffusion currents at a scan rate of 0.8 mV·s^{-1}. (d) Contribution ratios of the capacitive and diffusion-controlled charge at various scan rates.

to be diffusion-controlled. The remaining regions are almost capacitive, which is consistent with the observed *b* value. The kinetic analysis shows that a large fraction of the stored charge comes from a capacitive process. Thus, it is not surprising that the rate-controlling step is surface-limited rather than solid-state diffusion [56–60]. These results clearly imply that the yolk–shell Co_3O_4/C dodecahedrons offer more efficient surface active sites because of their large specific surface area, resulting in an enhanced capacity and rate performance [59, 60].

To further demonstrate the structural superiority of the yolk–shell Co_3O_4/C dodecahedrons, the electrochemical properties of SIBs were also studied. First, the CV curves of the electrodes were characterized in the range of 0.01 to 3 V vs. Na^+/Na at a scan rate of 0.1 $mV\cdot s^{-1}$ (Fig. 6(a)). During the first cathodic scan, only one intense peak around 0.5 V was observed, which is assigned to the reduction of Co_3O_4 to Co and the simultaneous formation of Na_2O and the SEI film [61]. For the anodic scan, the strong peak at ~1.75 V is ascribed to the reoxidation of metallic Co [49]. These

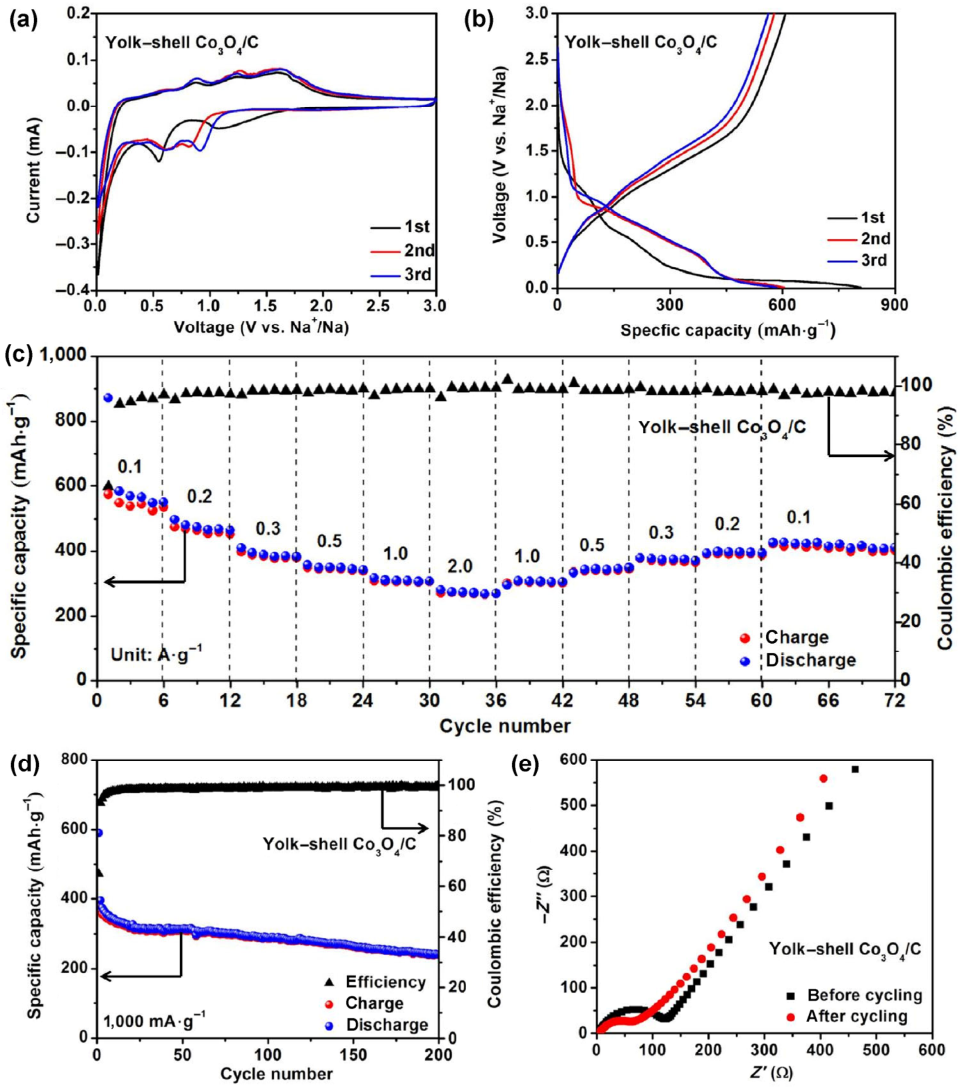

Figure 6 Electrochemical performances of the yolk–shell Co_3O_4/C dodecahedrons in SIBs: (a) CV curves of the yolk–shell Co_3O_4/C dodecahedrons collected at a scan rate of 0.1 $mV\cdot s^{-1}$ within the voltage range of 0.01–3 V. (b) Galvanostatic charge/discharge profiles for the first three cycles at a current density of 200 $mA\cdot g^{-1}$. (c) Rate capability tested at rates ranging from 0.1 to 2.0 $A\cdot g^{-1}$. (d) Capacity and Coulombic efficiency vs. the cycle number for the yolk–shell Co_3O_4/C dodecahedrons at a current density of 1,000 $mA\cdot g^{-1}$. (e) EIS plots of yolk–shell Co_3O_4/C dodecahedrons before and after 50 cycles in the frequency range of 0.01 Hz to 100 kHz.

electrochemical details are consistent with the results reported by Rahman et al. [61], who found that the electrochemical sodiation/desodiation of nanostructured Co_3O_4 is a partial conversion process, as shown in Fig. S12 in the ESM. The yolk–shell Co_3O_4/C dodecahedrons delivered discharge and charge capacities of 808 and 608 mAh·g^{-1}, respectively, when SIBs were cycled at a current density of 200 mA·g^{-1} (Fig. 6(b)). Average discharge capacities of 551, 465, 383, 342, 307, and 269 mAh·g^{-1} were obtained at current densities of 100, 200, 300, 500, 1,000, and 2,000 mA·g^{-1}, respectively (Fig. 6(c)). In addition to the excellent high-rate performance, the materials exhibited good cycling stability. At a current density of 1,000 mA·g^{-1}, the second discharge capacity was 395 mAh·g^{-1}, and a capacity of 240 mAh·g^{-1} was achieved even after 200 cycles, indicating the good capacity retention of the yolk–shell Co_3O_4/C dodecahedrons. The corresponding galvanostatic charge/discharge profiles of the yolk–shell Co_3O_4/C dodecahedrons in SIBs are shown in Fig. S11 in the ESM. Nyquist plots for the dodecahedrons before and after 50 cycles present a semicircle and a quasi-straight line, respectively, which are associated with the charge-transfer resistance (R_{ct}) and the impedance of the Na^+ diffusion in solid materials, respectively (Fig. 6(d)). The R_{ct} decreased after the charging/discharging of the electrode, indicating a decrease in resistance after cycling. Additionally, the slope in the low-frequency range increased, indicating enhanced ion-diffusion kinetics. The rate performance and the specific capacity of yolk–shell Co_3O_4/C dodecahedrons in SIBs are comparable to previously reported results [62–64] (Table S2 in the ESM), while the composites show a lower capacity in SIBs than in LIBs. The results indicate relatively inferior sodium-storage kinetics due to the higher diffusion barrier of sodium ions, which is commonly observed for the sodium versions of lithium-ion intercalation materials [65, 66] and is supported by theoretical calculations [67].

The aforementioned findings indicate that the excellent Li/Na storage capability is derived from the following properties of the yolk–shell Co_3O_4/C dodecahedrons. First, the carbon matrix can enhance the conductivity of the active material. Second, the unique yolk–shell structure and the large specific surface area provide an ideal environment for the electrolyte penetration and for mitigating the volume expansion during the lithiation/sodiation process. According to the aforementioned analysis and electrochemical performances, the as-prepared yolk–shell Co_3O_4/C dodecahedrons have great potential as anodes for LIBs and SIBs.

4 Conclusions

We demonstrate a facile interface-modulated method for synthesizing carbon-based metal-oxide composites with a yolk–shell structure by controlling the heat-treatment process. Compared with the bulk structure, this unique hierarchically porous yolk–shell structure provides more abundant channels and sites, a larger contact area, and better strain accommodation. In addition, the supporting carbon matrix enhances the conductivity of the electrode. Benefiting from these unique features, the yolk–shell Co_3O_4/C dodecahedrons in LIBs exhibit a high specific capacity and excellent cycling performance. SIBs with the yolk–shell Co_3O_4/C dodecahedrons display an outstanding rate capability. Detailed electrochemical kinetic analysis of the yolk–shell Co_3O_4/C dodecahedrons indicates that energy storage for Li^+ and Na^+ shows a dominant capacitive behavior. This work demonstrates a facile method for fabricating carbon-based hollow structures derived from MOFs, and these multifunctional architectures have great potential for use in electrochemical energy-storage systems.

Acknowledgements

This work was supported by the National Key Research and Development Program of China (No. 2016YFA0202603), the National Basic Research Program of China (No. 2013CB934103), the National Natural Science Foundation of China (Nos. 51521001 and 51272197), the National Natural Science Fund for Distinguished Young Scholars (No. 51425204), the Fundamental Research Funds for the Central Universities (WUT: 22016III001, 2017IVA096) and the Foundation of National Excellent Doctoral Dissertation of PR China (No. 2016-YB-004); Prof. Liqiang Mai gratefully acknowledges the financial support from China Scholarship Council (No. 201606955096).

Electronic Supplementary Material: Supplementary material (nitrogen adsorption–desorption isotherms and corresponding pore size distribution of ZIF-67, TG curves of ZIF-67; XRD pattern and SEM image of Co_3O_4-B, TEM images, XPS survey spectra, Raman spectrum, TG curve and nitrogen adsorption–desorption isotherms and corresponding pore size distribution of yolk–shell Co_3O_4/C and electrochemical performances of yolk–shell Co_3O_4/C; XRD patterns and SEM images of yolk–shell NiO/C microsphere) is available in the online version of this article at http://dx.doi.org/10.1007/s12274-017-1433-6.

References

[1] Chu, S.; Majumdar, A. Opportunities and challenges for a sustainable energy future. *Nature* **2012**, *488*, 294–303.

[2] Liu, J. Addressing the grand challenges in energy storage. *Adv. Funct. Mater.* **2013**, *23*, 924–928.

[3] Wei, W.; Wang, Y. C.; Wu, H.; Al-Enizi, A. M.; Zhang, L. J.; Zheng, G. F. Transition metal oxide hierarchical nanotubes for energy applications. *Nanotechnology* **2016**, *27*, 02LT01.

[4] Dunn, B.; Kamath, H.; Tarascon, J. M. Electrical energy storage for the grid: A battery of choices. *Science* **2011**, *334*, 928–935.

[5] Pasta, M.; Wessells, C. D.; Huggins, R. A.; Cui, Y. A high-rate and long cycle life aqueous electrolyte battery for grid-scale energy storage. *Nat. Commun.* **2012**, *3*, 1149.

[6] Suo, L. M.; Hu, Y. S.; Li, H.; Armand, M.; Chen, L. Q. A new class of solvent-in-salt electrolyte for high-energy rechargeable metallic lithium batteries. *Nat. Commun.* **2013**, *4*, 1481.

[7] Yang, C. P.; Yin, Y. X.; Zhang, S. F.; Li, N. W.; Guo, Y. G. Accommodating lithium into 3D current collectors with a submicron skeleton towards long-life lithium metal anodes. *Nat. Commun.* **2015**, *6*, 8058.

[8] Ding, Y. L.; Wen, Y. R.; Wu, C.; van Aken, P. A.; Maier, J.; Yu, Y. 3D V_6O_{13} nanotextiles assembled from interconnected nanogrooves as cathode materials for high-energy lithium ion batteries. *Nano Lett.* **2015**, *15*, 1388–1394.

[9] Zhu, C. B.; Mu, X. K.; van Aken, P. A.; Maier, J.; Yu, Y. Fast Li storage in MoS_2-graphene-carbon nanotube nanocomposites: Advantageous functional integration of 0D, 1D, and 2D nanostructures. *Adv. Energy Mater.* **2015**, *5*, 1401170.

[10] Chen, Y. M.; Yu, L.; Lou, X. W. Hierarchical tubular structures composed of Co_3O_4 hollow nanoparticles and carbon nanotubes for lithium storage. *Angew. Chem.* **2016**, *128*, 6094–6097.

[11] Ji, L. W.; Lin, Z.; Alcoutlabi, M.; Zhang, X. W. Recent developments in nanostructured anode materials for rechargeable lithium-ion batteries. *Energy Environ. Sci.* **2011**, *4*, 2682–2699.

[12] Yuan, S.; Wang, S.; Li, L.; Zhu, Y. H.; Zhang, X. B.; Yan, J. M. Integrating 3D flower-like hierarchical Cu_2NiSnS_4 with reduced graphene oxide as advanced anode materials for Na-ion batteries. *ACS Appl. Mater. Interfaces* **2016**, *8*, 9178–9184.

[13] Wang, S.; Yuan, S.; Yin, Y. B.; Zhu, Y. H.; Zhang, X. B.; Yan, J. M. Green and facile fabrication of MWNTs@Sb_2S_3@PPy coaxial nanocables for high-performance Na-ion batteries. *Part. Part. Syst. Char.* **2016**, *33*, 493–499.

[14] Huang, X. L.; Zhao, X.; Wang, Z. L.; Wang, L. M.; Zhang, X. B. Facile and controllable one-pot synthesis of an ordered nanostructure of $Co(OH)_2$ nanosheets and their modification by oxidation for high-performance lithium-ion batteries. *J. Mater. Chem.* **2012**, *22*, 3764–3769.

[15] Huang, X. L.; Wang, R. Z.; Xu, D.; Wang, Z. L.; Wang, H. G.; Xu, J. J.; Wu, Z.; Liu, Q. C.; Zhang, Y.; Zhang, X. B. Homogeneous CoO on graphene for binder-free and ultralong-life lithium ion batteries. *Adv. Funct. Mater.* **2013**, *23*, 4345–4353.

[16] Yu, Y.; Niu, C. J.; Han, C. H.; Zhao, K. N.; Meng, J. S.; Xu, X. M.; Zhang, P. F.; Wang, L.; Wu, Y. Z.; Mai, L. Q. Zinc pyrovanadate nanoplates embedded in graphene networks with enhanced electrochemical performance. *Ind. Eng. Chem. Res.* **2016**, *55*, 2992–2999.

[17] Mahmood, N.; Zhu, J. H.; Rehman, S.; Li, Q.; Hou, Y. L. Control over large-volume changes of lithium battery anodes via active–inactive metal alloy embedded in porous carbon. *Nano Energy* **2015**, *15*, 755–765.

[18] Roh, H. K.; Kim, H. K.; Kim, M. S.; Kim, D. H.; Chung, K. Y.; Roh, K. C.; Kim, K. B. *In situ* synthesis of chemically bonded $NaTi_2(PO_4)_3$/rGO 2D nanocomposite for high-rate sodium-ion batteries. *Nano Res.* **2016**, *9*, 1844–1855.

[19] Xie, D.; Tang, W. J.; Wang, Y. D.; Xia, X. H.; Zhong, Y.; Zhou, D.; Wang, D. H.; Wang, X. L.; Tu, J. P. Facile fabrication of integrated three-dimensional C-$MoSe_2$/reduced graphene oxide composite with enhanced performance for sodium storage. *Nano Res.* **2016**, *9*, 1618–1629.

[20] Wang, X. P.; Niu, C. J.; Meng, J. S.; Hu, P.; Xu, X. M.; Wei, X. J.; Zhou, L.; Zhao, K. N.; Luo, W.; Yan, M. Y. et al. Novel $K_3V_2(PO_4)_3$/C bundled nanowires as superior sodium-ion battery electrode with ultrahigh cycling stability. *Adv. Energy Mater.* **2015**, *5*, 1500716.

[21] Niu, C. J.; Meng, J. S.; Wang, X. P.; Han, C. H.; Yan, M. Y.; Zhao, K. N.; Xu, X. M.; Ren, W. H.; Zhao, Y. L.; Xu, L. et al. General synthesis of complex nanotubes by

gradient electrospinning and controlled pyrolysis. *Nat. Commun.* **2015**, *6*, 7402.

[22] Lee, J.; Zhu, H. Z.; Yadav, G. G.; Caruthers, J.; Wu, Y. Porous ternary complex metal oxide nanoparticles converted from core/shell nanoparticles. *Nano Res.* **2016**, *9*, 996–1004.

[23] Sun, C. C.; Dong, Q. C.; Yang, J.; Dai, Z. Y.; Lin, J. J.; Chen, P.; Huang, W.; Dong, X. C. Metal–organic framework derived $CoSe_2$ nanoparticles anchored on carbon fibers as bifunctionalelectrocatalysts for efficient overall water splitting. *Nano Res.* **2016**, *9*, 2234–2243.

[24] Meng, J. S.; Niu, C. J.; Liu, X.; Liu, Z. A.; Chen, H. L.; Wang, X. P.; Li, J. T.; Chen, W.; Guo, X. F.; Mai, L. Q. Interface-modulated approach toward multilevel metal oxide nanotubes for lithium-ion batteries and oxygen reduction reaction. *Nano Res.* **2016**, *9*, 2445–2457.

[25] Wang, Z.; Jia, W.; Jiang, M. L.; Chen, C.; Li, Y. D. One-step accurate synthesis of shell controllable $CoFe_2O_4$ hollow microspheres as high-performance electrode materials in supercapacitor. *Nano Res.* **2016**, *9*, 2026–2033.

[26] Wang, S. B.; Xing, Y. L.; Xu, H. Z.; Zhang, S. C. MnO nanoparticles interdispersed in 3D porous carbon framework for high performance lithium-ion batteries. *ACS Appl. Mater. Interfaces* **2014**, *6*, 12713–12718.

[27] Kim, W. S.; Choi, J.; Hong, S. H. Meso-porous silicon-coated carbon nanotube as an anode for lithium-ion battery. *Nano Res.* **2016**, *9*, 2174–2181.

[28] Jiao, J. Q.; Qiu, W. D.; Tang, J. G.; Chen, L. P.; Jing, L. Y. Synthesis of well-defined Fe_3O_4 nanorods/N-doped graphene for lithium-ion batteries. *Nano Res.* **2016**, *9*, 1256–1266.

[29] Yang, J.; Zhang, Y.; Sun, C. C.; Liu, H. Z.; Li, L. Q.; Si, W. L.; Huang, W.; Yan, Q. Y.; Dong, X. C. Graphene and cobalt phosphide nanowire composite as an anode material for high performance lithium-ion batteries. *Nano Res.* **2016**, *9*, 612–621.

[30] Luo, B.; Zhi, L. J. Design and construction of three dimensional graphene-based composites for lithium ion battery applications. *Energy Environ. Sci.* **2015**, *8*, 456–477.

[31] Niu, C. J.; Huang, M.; Wang, P. Y.; Meng, J. S.; Liu, X.; Wang, X. P.; Zhao, K. N.; Yu, Y.; Wu, Y. Z.; Lin, C. et al. Carbon-supported and nanosheet-assembled vanadium oxide microspheres for stable lithium-ion battery anodes. *Nano Res.* **2016**, *9*, 128–138.

[32] Jeong, J. M.; Choi, B. G.; Lee, S. C.; Lee, K. G.; Chang, S. J.; Han, Y. K.; Lee, Y. B.; Lee, H. U.; Kwon, S.; Lee, G. et al. Hierarchical hollow spheres of Fe_2O_3@polyaniline for lithium ion battery anodes. *Adv. Mater.* **2013**, *25*, 6250–6255.

[33] Wang, N.; Liu, Q. L.; Kang, D. M.; Gu, J. J.; Zhang, W.; Zhang, D. Facile self-cross-linking synthesis of 3D nanoporous Co_3O_4/carbon hybrid electrode materials for supercapacitors. *ACS Appl. Mater. Interfaces* **2016**, *8*, 16035–16044.

[34] Xu, X. D.; Cao, R. G.; Jeong, S.; Cho, J. Spindle-like mesoporous α-Fe_2O_3 anode material prepared from MOF template for high-rate lithium batteries. *Nano Lett.* **2012**, *12*, 4988–4991.

[35] Shao, J.; Wan, Z. M.; Liu, H. M.; Zheng, H. Y.; Gao, T.; Shen, M.; Qu, Q. T.; Zheng, H. H. Metal organic frameworks-derived Co_3O_4 hollow dodecahedrons withcontrollable interiors as outstanding anodes for Li storage. *J. Mater. Chem. A* **2014**, *2*, 12194–12200.

[36] Zhang, L.; Wu, H. B.; Madhavi, S.; Hng, H. H.; Lou, X. W. Formation of Fe_2O_3 microboxes with hierarchical shell structures from metal-organic frameworks and their lithium storage properties. *J. Am. Chem. Soc.* **2012**, *134*, 17388–17391.

[37] Han, Y.; Zhao, M. L.; Dong, L.; Feng, J. M.; Wang, Y. J.; Li, D. J.; Li, X. F. MOF-derived porous hollow Co_3O_4 parallelepipeds for building high-performance Li-ion batteries. *J. Mater. Chem. A***2015**, *3*, 22542–22546.

[38] Tian, D.; Zhou, X. L.; Zhang, Y. H.; Zhou, Z.; Bu, X. H. MOF-derived porous Co_3O_4 hollow tetrahedra with excellent performance as anode materials for lithium-ion batteries. *Inorg. Chem.* **2015**, *54*, 8159–8161.

[39] Hou, Y.; Li, J. Y.; Wen, Z. H.; Cui, S. M.; Yuan, C.; Chen, J. H.Co_3O_4 nanoparticles embedded in nitrogen-doped porous carbon dodecahedrons with enhanced electrochemical properties for lithium storage and water splitting. *Nano Energy* **2015**, *12*, 1–8.

[40] Zou, F.; Chen, Y. M.; Liu, K. W.; Yu, Z. T.; Liang, W. F.; Bhaway, S. M.; Gao, M.; Zhu, Y. Metal organic frameworks derived hierarchical hollow NiO/Ni/graphene composites for lithium and sodium storage. *ACS Nano* **2016**, *10*, 377–386.

[41] Jiang, Z.; Li, Z. P.; Qin, Z. H.; Sun, H. Y.; Jiao, X. L.; Chen, D. R. LDH nanocages synthesized with MOF templates and their high performance as supercapacitors. *Nanoscale* **2013**, *5*, 11770–11775.

[42] Zhou, L.; Zhao, D. Y.; Lou, X. W. Double-shelled $CoMn_2O_4$ hollow microcubes as high-capacity anodes for lithium-ion batteries. *Adv. Mater.* **2012**, *24*, 745–748.

[43] Yan, N.; Hu, L.; Li, Y.; Wang, Y.; Zhong, H.; Hu, X. Y.; Kong, X. K.; Chen, Q. W. Co_3O_4 nanocages for high-performance anode material in lithium-ion batteries. *J. Phys. Chem. C* **2012**, *116*, 7227–7235.

[44] Li, W. Y.; Xu, L. N.; Chen, J. Co_3O_4 nanomaterials in lithium-ion batteries and gas sensors. *Adv. Funct. Mater.* **2005**, *15*, 851–857.

[45] Du, N.; Zhang, H.; Chen, B. D.; Wu, J. B.; Ma, X. Y.; Liu, Z. H.; Zhang, Y. Q.; Yang, D. R.; Huang, X. H.; Tu, J. P. Porous Co_3O_4 nanotubes derived from $Co_4(CO)_{12}$ clusters on carbon nanotube templates: A highly efficient material for Li-battery applications. *Adv. Mater.* **2007**, *19*, 4505–4509.

[46] Grugeon, S.; Laruelle, S.; Dupont, L.; Tarascon, J. M. An update on the reactivity of nanoparticles Co-based compounds towards Li. *Solid State Sci.* **2003**, *5*, 895–904.

[47] Lee, J. E.; Yu, S. H.; Lee, D. J.; Lee, D. C.; Han, S. I.; Sung, Y. E.; Hyeon, T. Facile and economical synthesis of hierarchical carbon-coated magnetite nanocomposite particles and their applications in lithium ion battery anodes. *Energy Environ. Sci.* **2012**, *5*, 9528–9533.

[48] Zheng, C.; Zhou, X. F.; Cao, H. L.; Wang, G. H.; Liu, Z. P. Synthesis of porous graphene/activated carbon composite with high packing density and large specific surface area for supercapacitor electrode material. *J. Power Sources* **2014**, *258*, 290–296.

[49] Choi, S. H.; Lee, J. K.; Kang, Y. C. Three-dimensional porous graphene-metal oxide compositemicrospheres: Preparation and application in Li-ion batteries. *Nano Res.* **2015**, *8*, 1584–1594.

[50] Fei, H. L.; Peng, Z. W.; Li, L.; Yang, Y.; Lu, W.; Samuel, E. L. G.; Fan, X. J.; Tour, J. M. Preparation of carbon-coated iron oxide nanoparticles dispersed on graphene sheets and applications as advanced anode materials for lithium-ion batteries. *Nano Res.* **2014**, *7*, 502–510.

[51] Huang, G.; Zhang, F. F.; Du, X. C.; Qin, Y. L.; Yin, D. M.; Wang, L. M. Metal organic frameworks route to *in situ* insertion of multiwalled carbon nanotubes in Co_3O_4 polyhedra as anode materials for lithium-ion batteries. *ACS Nano* **2015**, *9*, 1592–1599.

[52] Qu, Q. T.; Gao, T.; Zheng, H. Y.; Li, X. X.; Liu, H. M.; Shen, M.; Shao, J.; Zheng, H. H. Graphene oxides-guided growth of ultrafine Co_3O_4 nanocrystallites from MOFs as high-performance anode of Li-ion batteries. *Carbon* **2015**, *92*, 119–125.

[53] Huang, G.; Zhang, F. F.; Du, X. C.; Wang, J. W.; Yin, D. M.; Wang, L. M. Core–shell $NiFe_2O_4$@TiO_2 nanorods: An anode material with enhanced electrochemical performance for lithium-ion batteries. *Chem.—Eur. J.* **2014**, *20*, 11214–11219.

[54] Muller, G. A.; Cook, J. B.; Kim, H. S.; Tolbert, S. H.; Dunn, B. High performance pseudocapacitor based on 2D layered metal chalcogenide nanocrystals. *Nano Lett.* **2015**, *15*, 1911–1917.

[55] Kim, H. S.; Cook, J. B.; Tolbert, S. H.; Dunn, B. The development of pseudocapacitive properties in nanosized-MoO_2. *J. Electrochem. Soc.* **2015**, *162*, A5083–A5090.

[56] Zhu, Y.; Peng, L. L.; Chen, D. H.; Yu, G. H. Intercalation pseudocapacitance in ultrathinVOPO$_4$ nanosheets: Toward high-rate alkali-ion-based electrochemical energy storage. *Nano Lett.* **2016**, *16*, 742–747.

[57] Wang, J.; Polleux, J.; James, L. A.; Dunn, B. Pseudocapacitive contributions to electrochemical energy storage in TiO_2 (anatase) nanoparticles. *J. Phys. Chem. C* **2007**, *111*, 14925–14931.

[58] Kim, H.; Hong, J.; Park, Y. U.; Kim, J.; Hwang, I.; Kang, K. Sodium storage behavior in natural graphite using ether-based electrolyte systems. *Adv. Funct. Mater.* **2015**, *25*, 534–541.

[59] Li, S.; Qiu, J. X.; Lai, C.; Ling, M.; Zhao, H. J.; Zhang, S. Q. Surface capacitive contributions: Towards high rate anode materials for sodium ion batteries. *Nano Energy* **2015**, *12*, 224–230.

[60] Zhao, K. N.; Liu, F. N.; Niu, C. J.; Xu, W. W.; Dong, Y. F.; Zhang, L.; Xie, S. M.; Yan, M. Y.; Wei, Q. L.; Zhao, D. Y. et al. Graphene oxide wrapped amorphous copper vanadium oxide with enhanced capacitive behavior for high-rate and long-life lithium-ion battery anodes. *Adv. Sci.* **2015**, *2*, 1500154.

[61] Rahman, M. M.; Glushenkov, A. M.; Ramireddy, T.; Chen, Y. Electrochemical investigation of sodium reactivity with nanostructured Co_3O_4 for sodium-ion batteries. *Chem. Commun.* **2014**, *50*, 5057–5060.

[62] Jian, Z. L.; Liu, P.; Li, F. J.; Chen, M. W.; Zhou, H. S. Monodispersed hierarchical Co_3O_4 spheres intertwined with carbon nanotubes for use as anode materials in sodium-ion batteries. *J. Mater. Chem. A* **2014**, *2*, 13805–13809.

[63] Liu, Y. G.; Cheng, Z. Y.; Sun, H. Y.; Arandiyan, H.; Li, J. P.; Ahmad, M. Mesoporous Co_3O_4 sheets/3D graphene networks nanohybrids for high-performance sodium-ion battery anode. *J. Power Sources* **2015**, *273*, 878–884.

[64] Yang, J. P.; Zhou, T. F.; Zhu, R.; Chen, X. Q.; Guo, Z. P.; Fan, J. W.; Liu, H. K.; Zhang, W. X. Highly ordered dual porosity mesoporous cobalt oxide for sodium-ion batteries. *Adv. Mater. Interfaces* **2016**, *3*, 1500464.

[65] Moreau, P.; Guyomard, D.; Gaubicher, J.; Boucher, F. Structure and stability of sodium intercalated phases in olivine $FePO_4$. *Chem. Mater.* **2010**, *22*, 4126–4128.

[66] Naeyaert, P. J. P.; Avdeev, M.; Sharma, N.; Yahia, H. B.; Ling, C. D. Synthetic, structural, and electrochemical study of monoclinic $Na_4Ti_5O_{12}$ as a sodium-ion battery anode material. *Chem. Mater.* **2014**, *26*, 7067–7072.

[67] Ong, S. P.; Chevrier, V. L.; Hautier, G.; Jain, A.; Moore, C.; Kim, S.; Ma, X. H.; Ceder, G. Voltage, stability and diffusion barrier differences between sodium-ion and lithium-ion intercalation materials. *Energy Environ. Sci.* **2011**, *4*, 3680–3688.